24 Quantitative Analysis of Surface Morphology and Applications

Maria Cecília Salvadori

Abstract. The quantitative analysis of surfaces using atomic force microscopy and scanning tunneling microscopy is described. Roughness, correlation length, fractal dimension, and power spectral density are discussed. A number of applications are presented, showing quantitative morphological analyses. The applications include investigations of the dynamic growth of thin films, periodicity of lines nanolithographed by AFM in PMMA, electrical resistivity of nanostructured thin films, and grain size analysis.

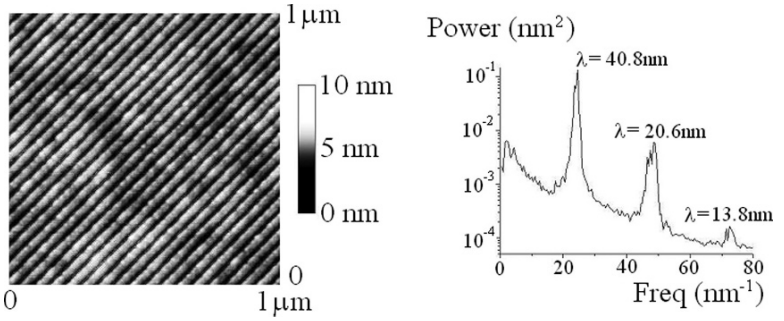

Key words: Roughness, Correlation length, Fractal dimension, Power spectral density, Dynamic growth, Nanolithography, Electrical resistivity, Grain size

24.1 Introduction

Atomic force microscopy (AFM) and Scanning Tunneling Microcopy (STM) are powerful tools for imaging surface morphology at high spatial resolution. The morphological analysis of surfaces can be extremely complex, however, it is not uncommon for these techniques to be only partially employed.

In this chapter we discuss quantitative parameters used to describe or analyze surfaces using AFM and STM. Parameters for quantification of surface morphology are introduced. Roughness is the most widely used parameter for quantitative characterization of surface morphology, but it adds limited information about the

surface and is scale dependent, meaning that in terms of scanning probe microscope (SPM) images, the derived roughness depends on the scan size (ℓ). The parameter ξ, defined as *correlation length*, is another important parameter used to quantitatively describe the surface. The area $\xi \times \xi$ is the minimum area of the surface that is representative of the entire surface. The concept of fractal dimension, d_f, is introduced and discussed as another quantitative parameter for surface morphology analysis. But the most complete method to quantify a surface morphologically is the Power Spectral Density (PSD). This technique involves basically a Fourier transform of the surface topography, displaying a graphic of the squared modulus (amplitude) of the Fourier transform (scaled by an appropriate constant) as a function of the morphological wavelength (or frequency). A number of applications are then presented, demonstrating some quantitative morphological analyses. The first application is the dynamic growth of thin films. This approach allows us to investigate various growth processes and associate them with universality classes. In addition, dynamic growth studies provide us with some important parameters for quantitatively describing the film surface, such as the correlation length ξ and fractal dimension d_f. The second application is a periodicity analysis of lines nanolithographed by AFM in PMMA. Nanolithography performed by AFM has been used to generate reproducible and predictable periodic morphology that is mainly dependent on the scan size and the number of scan lines. A PSD characterization provides in this case a powerful method to identify the morphological wavelengths present in the nanolithographed pattern. The third application is a study of the electrical resistivity of nanostructured thin films. The electrical resistivity of thin films is best described by a quantum model, when appropriate conditions are satisfied. In this model, conduction electrons are scattered by the surface morphology and quantitative morphological analysis of the film surface is fundamental to the model. Related to this application, we also explore the resistivity anisotropy that can be induced by film surface morphological anisotropy. Finally, the last application that we consider is the quantitative grain size analysis of surface morphology and its importance in some specific areas. In this context we define and discuss "morphological grain size" and "crystallographic grain size."

24.2 Quantifying Morphology

Roughness is the most commonly used parameter for characterizing surface morphology quantitatively, but surprisingly it provides incomplete information about the surface. To exemplify the limitations of this parameter, let us calculate the roughness of a simple surface (see Fig. 24.1) defined by a sinusoidal profile in the x direction and flat in the y direction. In this case the roughness can be taken as

$$\omega_{RMS} = \sqrt{\frac{\int_{x_1}^{x_2} [f(x) - < f(x) >]^2 dx}{x_2 - x_1}}$$

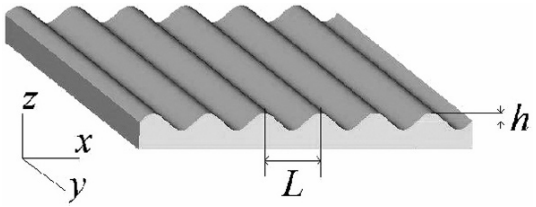

Fig. 24.1. Surface defined by a sinusoidal profile in the x direction and flat in the y direction. The amplitude of the sinusoidal profile is h and its morphological wavelength is L

where $f(x) = h\ \sin(2\pi x/L)$, h being the amplitude of the sinusoidal profile and L the morphological wavelength. Integrating over an integral number of cycles, we obtain $\omega_{RMS} = {}^{h}/_{\sqrt{2}}$. This result indicates clearly that the roughness of the surface shown in Fig. 24.1 depends only on the amplitude h and is independent of the morphological wavelength L. Embarrassingly, we conclude that two surfaces like that shown in Fig. 24.1, having the same amplitude h but with different wavelengths L, for example with cross sections as shown in Fig. 24.2, will have exactly the same roughness.

Although roughness is thus a parameter carrying limited information, it nevertheless still plays an important role in morphology characterization. Let us consider roughness further.

For a self-affine surface [1–12], as is the case for most "real surfaces," the roughness is scale-dependent. In terms of SPM image acquisition, the roughness depends on the scan size (ℓ). Figure 24.3 illustrates the behavior of self-affine surface roughness as a function of ℓ. We verify that the roughness increases as ℓ increases and that the roughness saturates for $\ell > \xi$. This distance ξ is a parameter named *surface correlation length* [1–13]. The correlation length ξ is a meaningful parameter for the quantitative description of a surface.

As will be seen in what follows, for $\ell << \xi$, the roughness $\omega(\ell, t) \sim \ell^{\alpha}$, where α is a parameter called *growth exponent* [1–12] and is related to the fractal dimension d_f of the surface by $d_f = 3 - \alpha$. The fractal dimension is itself an important parameter for quantitative surface morphology analysis and will be discussed below.

The most complete method to quantify surface morphology is through its Power Spectral Density (PSD) [14]. This technique utilizes a Fourier transform of the surface topography, displaying a graphic of the squared modulus (amplitude h) of the

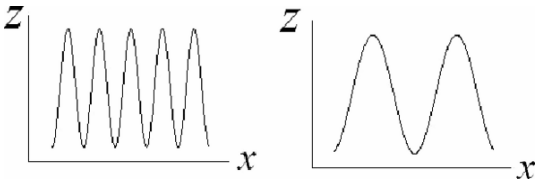

Fig. 24.2. Cross sections of two different surfaces with the same amplitude h and with different wavelengths L. These surfaces have the same roughness $\omega_{RMS} = {}^{h}/_{\sqrt{2}}$

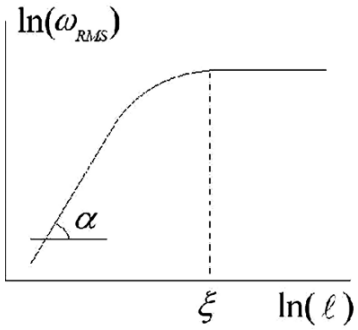

Fig. 24.3. Illustration of the behavior of self-affine surface roughness as a function of the image scan size (ℓ), where ξ is the surface *correlation length* and α is a growth exponent

Fourier transform (scaled by an appropriate constant factor) as a function of the morphological wavelength (or frequency). The PSD is expressed in squared length units (for example nm^2) and can be related to the roughness ω_{RMS} (associated with a given wavelength) and to the amplitude h of the surface Fourier transform by PSD $\propto \omega_{RMS}^2 \propto h^2$. Two examples of PSD analysis are shown in Fig. 24.4. These analyses were performed with the NanoScope IIIA software, version 5.30r3.sr3, from Veeco. For most "real surfaces," the amplitude increases with morphological wavelength, as illustrated in the examples of Fig. 24.4. The PSD analysis presented in Fig. 24.4a was performed with a homogeneous and isotropic rough surface, generating a broad band. Figure 24.4b shows a PSD analysis with pronounced peaks; in this case the surface was anisotropic with parallel lines, defining specific morphological frequencies (or wavelengths) as displayed in the analysis.

In the following we present a number of studies for which quantitative morphological analyses were carried out using the parameters introduced.

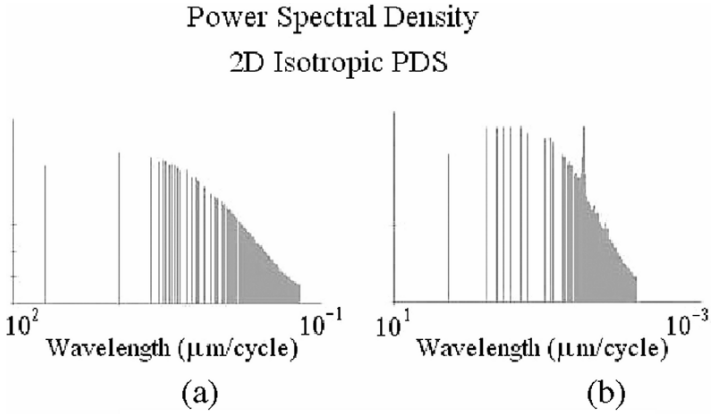

Fig. 24.4. Power Spectral Density (PSD) analysis for two different surfaces. (**a**) PSD for a homogeneous and isotropic surface, generating a broad band. (**b**) PSD with pronounced peaks, indicating the presence of specific morphological frequencies (or wavelengths)

24.3 Applications of Quantitative Morphological Surface Analysis

24.3.1 Dynamic Growth of Thin Films

Film growth by deposition is clearly of great technological importance. Fluctuations in the height $h(\mathbf{x}, t)$, surface location $\mathbf{x}$, and time t can be measured directly using a scanning probe microscope or indirectly by scattering. Analytical and numerical treatments of simple growth models suggest that, quite generally, the height fluctuations have a self-similar character and their average correlations exhibit a dynamic scaling form, named the Family-Vicsek scaling relationship [15]. The roughness ω and dynamic growth exponents α and z defined by this relationship are expected to be universal, depending only on the underlying mechanism that generates the self-similar scaling [16]. The determination of the growth exponents α and z is a fundamental problem of statistical mechanics. Considerable effort, both theoretical and experimental, has been made to investigate the surface growth process. Many references on the subject can be found in the excellent review of Barabási and Stanley [1]. Theoretical discrete models provided a substantial part of the driving force behind early investigations of the surface morphology. Discrete models, numerical simulations, and stochastic differential equations have been used to explain the growth mechanisms on d-dimensional substrates. Such equations typically describe the surface at large scales and times, which means that the short-range scale details are neglected and the focus is only on asymptotic coarse-grained (hydrodynamic) variables. In some sense, for $d = 1$ the growth phenomenon is reasonably well understood. Moreover, for $d > 1$, there are many challenging problems that seem insurmountable. Numerical simulations are generally impracticable or extremely difficult and numerical integrations are questionable, leading to somewhat inconclusive results [1–16]. On the other hand, more detailed and accurate measurements of the growth exponents of thin films are still lacking, and experimental confirmation of dynamic scaling is scarce [16, 17].

To exemplify a typical experimental approach for measuring the growth parameters of thin films, we describe a study of diamond films synthesized by microwave plasma-assisted chemical vapor deposition [18]. The roughness and dynamic exponents of these films were measured using atomic force microscopy.

The equipment used for the diamond film deposition is described in detail elsewhere [19, 20]. The substrate was silicon that had been scratched by 1-μm diamond powder and cleaned in an acetone ultrasonic bath. The following growth parameters were used: 300 sccm hydrogen flow rate (where sccm denotes cubic centimeter per minute at STP), 1.5 sccm methane flow rate (0.5-vol% methane in hydrogen), 70 torr chamber pressure, 820 °C substrate temperature, and nominal 850-W microwave power. The silicon substrate was divided into small pieces and eight films were synthesized with different growth times: 17, 20, 24, 26, 34, 48, 63, and 74 h.

The most economical way to characterize self-affine roughness is by a dynamic scaling form [15, 16]. In many situations, there is no information about the dynamics of the growth and it is not possible to produce surfaces with different sizes. Suppose

that the only data available are collected at the final stage of the experiment, consisting of the values of the height $h(\mathbf{x}, t)$ of the surface, at different points $\mathbf{x}$ and times t. In this situation, the scaling of the "local roughness" $\omega_L(\ell,\ t)$ is studied, defined by [15]

$$\omega_L^2(\ell, t) = \left\langle [h(\mathbf{x}, t) - h_\ell(\mathbf{x}, t)]^2 \right\rangle_{\mathbf{x}}$$

where $L \times L$ is the system size, $\ell \times \ell$ is a window selected on the surface and $h_\ell(\mathbf{x}, t)$ is the average height in this window. The angular brackets $\langle\rangle_{\mathbf{x}}$ denote spatial (over $\mathbf{x}$) and ensemble averages. One can show that $\omega_L(\ell,\ t)$ obeys the scaling form [1,15,16]

$$\omega_L^2(\ell, t) \sim \ell^{\alpha} f(t/\ell^z), \tag{24.1}$$

where $f(u)$ is the scaling function of the argument $u = t/\ell^z$ and $z = \alpha/\beta$. The parameters $\alpha,\ \beta$, and z are expected to be universal parameters, named growth exponents. For very small times, $u << 1$, we have $\omega_L(\ell,\ t) \sim t^{\beta}$ when the roughness grows as t^{β} and the different sites of the surface are practically independent. As time increases, different sites on the surface begin to be correlated. The typical distance over which the heights "know about" each other, the characteristic distance over which they are correlated, is called the correlation length and is denoted by $\xi(t)$, a parameter already mentioned, which increases as $\xi(t) \sim t^{1/z}$. When correlations are significant we have $\omega_L(\ell,\ t) \sim \ell^{\alpha}$ for $\ell << \xi$; for $\ell > \xi$ the roughness saturates, that is, $\omega_L(\ell,\ t) \cong \text{const} \sim \xi^{\alpha}$. For these conditions [1–12] the fractal dimension d_f of the film surface is given by $d_f = 3 - \alpha$. In the very long time limit, that is, as $u \to \infty$, it is expected that the roughness reaches its maximum (saturation) value $\omega_{\text{sat}}(L) \sim L^{\alpha}$. In what follows, omitting for simplicity the index L, the roughness will be indicated by $\omega(\ell,\ t)$; ℓ will be measured in micrometers and ω in nanometers.

The roughness and fractal dimensions of the seven diamond films were measured using an AFM, a Veeco NanoScope IIIA. Ten different regions of each sample were analyzed, each of size $160 \times 160\,\mu\text{m}^2$. Using the AFM zoom facility, these $(160 \times 160)\,\mu\text{m}^2$ regions were divided into smaller regions (windows) of size $\ell \times \ell\ \mu\text{m}^2$, with ℓ ranging from 3 up to $160\,\mu\text{m}$, and their local roughness $\omega(\ell,\ t)$ measured. It was not possible to analyze the 74-h sample due to the formation of large microcrystalline diamond grains, about $8.5\,\mu\text{m}$ in diameter; it was found that $\omega = 600\,\text{nm}$, exceeding the z limit of the AFM. The average grain sizes were about 2.8 and $7.0\,\mu\text{m}$ for 17 and 63 h, respectively.

Figure 24.5 shows typical values of $\log_{10}\omega(\ell,\ t)$ as a function of $\log_{10}(\ell)$ for different growth times t. One can verify that for $t < 34\,\text{h}$, the correlations between different sites of the surface are small and the α power law growth is not well defined. To determine the exponent α only the roughness of the 63-h sample was taken into account. Twelve different regions of this sample were analyzed. Figure 24.6 shows $\log_{10}[\omega(\ell,\ t = 63\,\text{h})]$ as a function of $\log_{10}(\ell)$ for these 12 regions. It can clearly be seen that $\log_{10}(\omega)$ as a function of $\log_{10}(\ell)$ shows a power law growth, appearing as a straight line from $3\,\mu\text{m}$ up to $\ell = \xi \cong 15\,\mu\text{m}$, where ξ is the correlation length. For $\ell \geq \xi$, the roughness saturates, that is, $\omega(\ell,\ t) \cong \text{const}$ according to Eq. (24.1), and is given by $\omega \cong 400\,\text{nm}$. The following α values were found for a straight line best fit [21] for the 12 different regions: $0.36 \pm 0.06,\ 0.49 \pm 0.04,\ 0.51 \pm 0.04,\ 0.51 \pm 0.08,\ 0.51 \pm 0.03,$

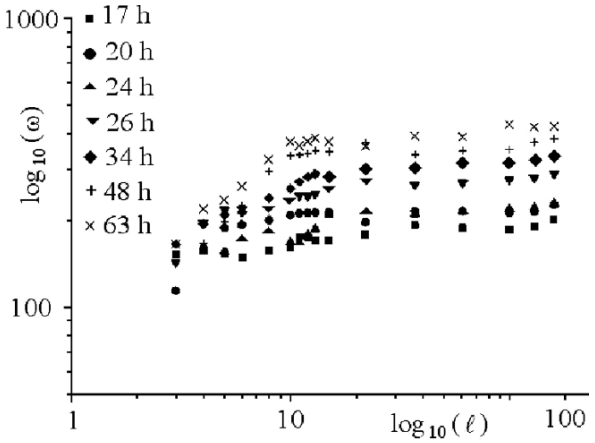

Fig. 24.5. Roughness $\omega(\ell,\ t)$ as a function of the length ℓ and of the growth time t; $\omega(\ell,\ t)$ is measured in nanometers, ℓ in micrometers, and t in hours

$0.53 \pm 0.03,\ 0.53 \pm 0.06,\ 0.58 \pm 0.07,\ 0.64 \pm 0.08,\ 0.66 \pm 0.11,\ 0.66 \pm 0.08,$ and 0.70 ± 0.10. To analyze the goodness of this straight line best fit we used a standard statistical procedure [21] calculating the χ^2_ν. The χ^2_ν values range from 0.97 up to 0.99, showing that the fit describes the data well. From the above α values we conclude that $\alpha = 0.56 \pm 0.09$.

The fractal dimension d_f of the 63-h sample was determined using the fractal algorithm of the AFM software, where the surface was analyzed as described below.

Let us now describe the surface fractal dimension [1–12]. A surface S can be measured by covering it with squares of linear dimension ℓ and area ℓ^2. $N(\ell)$ squares are needed to cover the surface, so $S(\ell) = N(\ell)\ell^2$. One might at first expect that for

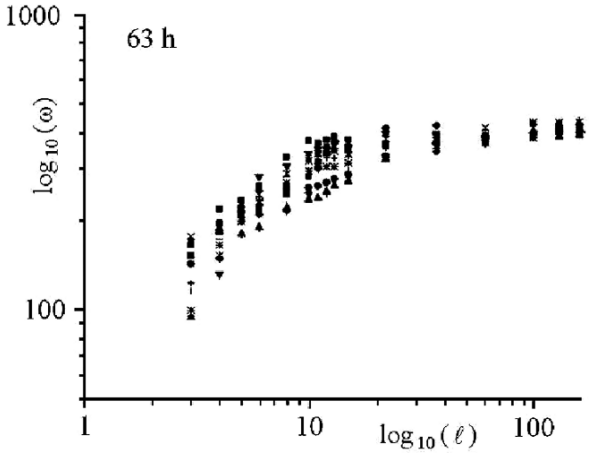

Fig. 24.6. Roughness $\omega(\ell,\ t = 63\,\mathrm{h})$ as a function of the length ℓ. The 12 different symbols for each curve correspond to the 12 different regions analyzed

a surface $N(\ell) \sim \ell^{-2}$, since the area of the surface does not change if we change the unit of measurement of ℓ. But for fractal surfaces we have $N(\ell) \sim \ell^{-d_f}$. Surfaces with $d_f > 2$ are fractal surfaces, where d_f is its fractal dimension.

Only the (160×160)-μm^2 images were considered. The following values were found for d_f: 2.43, 2.45, 2.46, 2.46, 2.47, 2.47, 2.48, 2.49, 2.49, 2.49, 2.50, and 2.50. So d_f would be given by $d_f = 2.48 \pm 0.02$ and consequently, as $\alpha = 3 - d_f$, α is given by $\alpha = 0.52 \pm 0.02$. This result is in good agreement with that obtained using the roughness measurement.

Figure 24.7 shows $\log_{10} \omega(t)$ as a function of $\log_{10}(t)$ for $t = 17$, 20, 24, 26, 34, 48, and 63 h. Since for small growth times [15] we must have $\omega \sim t^{\beta}$, determination of the growth exponent β takes into account the roughness of the samples only for small growth times, that is, 17, 20, and 24 h: $\omega(17\,\text{h}) = 205.7 \pm 6.9$ nm, $\omega(20\,\text{h}) = 219.63 \pm 7.2$ nm and $\omega(24\,\text{h}) = 232.0 \pm 4.9$ nm. These values were estimated from the average $\omega(t) = [\omega(100\,\mu\text{m}, t) + \omega(130\,\mu\text{m}, t) + \omega(160\,\mu\text{m}, t)]/3$. With a straight-line best fit [21], the growth exponent is given by $\beta = 0.34 \pm 0.02$. Also in this case, estimating the variances and χ^2_v indicates that $\chi^2_v = 0.99$, showing that a straight-line fit provides a good description of the data.

Taking into account the above values for α and β, we obtain $z = \alpha/\beta = 1.65 \pm 0.28$. Consequently $\alpha + z = 2.21 \pm 0.30$, which satisfies the condition $\alpha + z = 2$ within experimental error. This could be an indication that the growth of diamond films is governed by the Kardar–Parisi–Zhang (KPZ) equation [1–12, 16, 22, 23]. However, according to the KPZ predictions, for $d = 2$ ballistic deposition [16], $\alpha \cong 0.38$ and $\beta \cong 0.24$. Thus $\alpha \cong 1/2$ and $\beta \cong 1/3$, which are the growth exponents predicted by the KPZ equation for $d = 1$. This could provide support for the superuniversality conjecture [24]. On the other hand, the above discrepancies could be a result of the formation of diamond microcrystallites, and in this case a somewhat different equation would govern the diamond film growth, as proposed by Hwa, Kardar, and Paczuski [25].

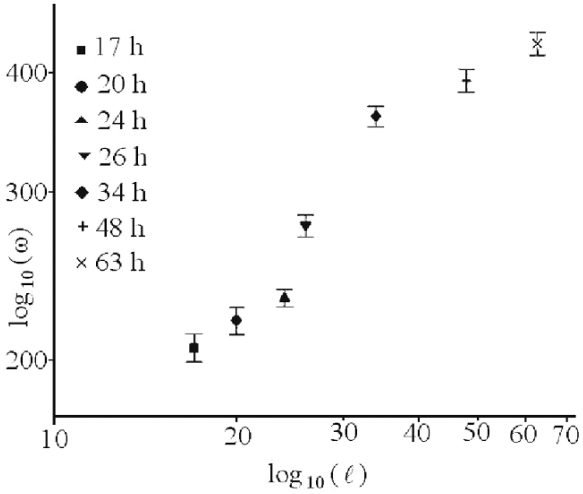

Fig. 24.7. Roughness $\omega(t)$ as a function of time t for $t = 17$, 20, 24, 26, 34, 48, and 63 h

Summarizing, dynamic growth of thin films allows us to investigate different growth processes and associate to universality classes. With this approach one can find a number of studies in the literature about growth dynamics of thin films [2–12]. In addition, a dynamic growth study yields important parameters for describing the film surfaces quantitatively, such as correlation length ξ and fractal dimension d_f.

24.3.2 Periodicity Analysis of Lines Nanolithographed by AFM in PMMA

An AFM can be used for imaging and also for creating surface nanostructures; this technique is called scanning probe lithography (SPL). A number of SPL techniques have been developed, based on nanomanipulation [26–28], mechanical modification [29–36], thermomechanical writing [37, 38], local oxidation [39–43], electron exposure of resistance [44–46], dip-pen nanolithography (DPN) [47–49], electrochemical dip-pen nanolithography (E-DPN) [50,51] and rapid direct nanowriting of a conducting polymer by electrochemical oxidative nanolithography [52].

Polymethylmethacrylate (PMMA) has been widely used as a photo- or electropositive resist for nano- and microscale fabrications. Thin, uniform layers of PMMA are deposited on a substrate and selected areas exposed to ultraviolet light or to a scanning electron beam. The irradiation creates scissions in molecular chains in the exposed areas of the polymer, decreasing their average molecular weight and allowing them to be removed through a development process. For nanodevice fabrication, it can be advantageous to form desired nanostructures on the PMMA surface after it has been irradiated and developed.

In the following we describe the application of an AFM nanolithography technique to mechanically modify PMMA surfaces previously irradiated and developed [29]. A quantitative analysis using AFM images will be presented.

Glass microscope slides were cut into $14 \times 5\text{-mm}^2$ pieces, cleaned and baked at 150 °C for 10 min to remove residual humidity, and PMMA then deposited on the samples using a spin coater. The samples were then baked again at 180 °C for 20 min to evaporate the polymer solvent. PMMA ARP671.06 was used, with molecular weight of 950,000 -g/mol and concentration of 6% in chlorobenzene, from Allresist. The average PMMA film thickness was 500 nm.

A selected area of the PMMA was electron beam scanned in a scanning electron microscope (JEOL model JSM-6460 LV) using an e-beam nanolithography system (Nanometer Pattern Generation System, NPGS) to create micropatterns that allowed subsequent identification and location of smaller nanostructures to be formed by AFM. The e-beam lithography was performed with a 30 kV, 50-pA electron beam. The applied electron dose was $225\,\text{C/cm}^2$ with an exposure time of $362\,\mu\text{s}$ at each scan point. The patterns consisted of two pads, each $20 \times 100\,\mu\text{m}^2$. The samples were then immersed in a developing solution of one-part methyl isobutyl ketone (MIBK): three-parts isopropyl alcohol (IPA) for 2 min and rinsed in IPA for 30 s.

The AFM used was a NanoScope IIIA with a tapping-mode probe. The procedure was to first obtain a tapping-mode image of a selected region, then to perform contact nanolithography, and finally to obtain a new tapping-mode image to visualize the modified surface. To image a surface using the NanoScope IIIA in AFM tapping

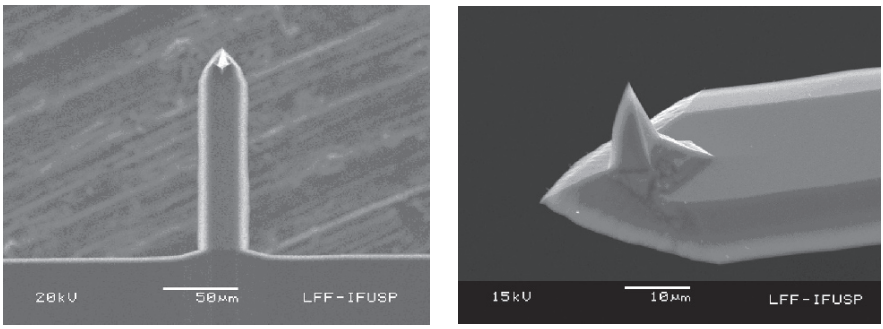

Fig. 24.8. SEM images of a typical AFM probe used for nanolithography. In the left image, low magnification, one can see the cantilever with a small pyramidal tip. In the right image, higher magnification, the pyramidal silicon tip can be seen

mode, the tip scans a maximum of 512 lines in a square area, interacting physically with 512 points along each of these lines. Importantly, note that the tip touches the surface only gently, and the polymer is not modified during image acquisition.

SEM images of a typical AFM probe used is shown in Fig. 24.8. The dimensions of each cantilever were measured (average dimensions were $120\,\mu m$ long, $33\,\mu m$ width, and $2.5\,\mu m$ thick), allowing calculation of its elastic constant [53]. A force plot was then obtained so as to precisely determine the cantilever deflection to be used in the lithography process. A typical deflection used was about 70 nm. In this way it was possible to define the force between the tip and the polymer. The force range was $0.5–1.0\,\mu N$.

Following calibration, the tip was engaged on the surface in contact mode and nanolithography initiated. The mechanism is similar to image acquisition, but with the scanning tip maintained in constant contact with the surface so as to scribe each scan line. The distance between two scan lines is the ratio between the scan size and the number of scan lines. For example, using a 20-μm scan size and 512 scan lines, the distance between the scan lines is about 39 nm. Note that for a Nanoscope IIIa the number of lines in each scan can be 512 or 256 or 128. In this study, the region was scanned just once, using 1-Hz scan rate and 0° scan angle. Finally, a tapping-mode image of the nanolithographed area was acquired, using a 45°-scan angle for better visualization of the surface morphology. The scan size, number of lines, and distance between lines for the nanolithographed patterns are shown in Table 24.1.

A typical AFM image of a nanolithographed PMMA region is shown in Fig. 24.9. Specifically in this case, the scan size and number of lines were $20\,\mu m$ and 512 lines, respectively. Consequently the distance between scan lines was 39.1 nm. The average morphological wavelengths present in this pattern were 39.2 nm and about half of this value, 19.4 nm. The reason for the occurrence of wavelengths of half the distance between scan lines is that the tip does not scan a single straight line, but technically follows a zigzag pattern. In other words, for each line the tip scans from left to right and from right to left, totaling two scratches for each line.

To characterize the morphological wavelengths present in each pattern formed by nanolithography we use the Power Spectral Density [54]. The PSD of the image

Table 24.1. Scan size, number of lines, and distance between lines for the nanolithographed patterns

Scan size (μm)	Number of lines	Distance between lines (nm)
10	512	19.5
20	512	39.1
20	256	78.1
30	512	58.6
40	512	78.1

shown in Fig. 24.9 is given in Fig. 24.10. The x-axis corresponds to the inverse of the wavelength (λ) and the y-axis is the PSD. The PSD is given in nm^2 and can be related to the roughness Δ (associated with each wavelength) and to the amplitude h of the surface Fourier transform as $\mathbf{PSD} \propto \Delta^2 \propto h^2$ [55]. The wavelength $\lambda = 13.8\,\mathrm{nm}$ in Fig. 24.10 is related to the tip radius due to the tip convolution, and will not be considered.

The sum of the PSD of nine different samples nanolithographed with 20-μm scan size and 512 lines is shown in Fig. 24.11. From this spectrum one can extract the average morphological wavelengths present for 20-μm scan size and 512 lines: 39.2 nm and 19.4 nm. The wavelength $\lambda = 12.9\,\mathrm{nm}$ in Fig. 24.11 is related to the tip radius.

The mechanism of the process is to move material from the region where the tip scratches the surface to the side of this region. In this way, the pattern profile obtained is higher than that of the original surface, as illustrated in Fig. 24.12. Note that in this last figure, the z-scale is 30 nm/division and the x and y-scale are 200 nm/division, so the image is expanded in the vertical direction to emphasize the image profile.

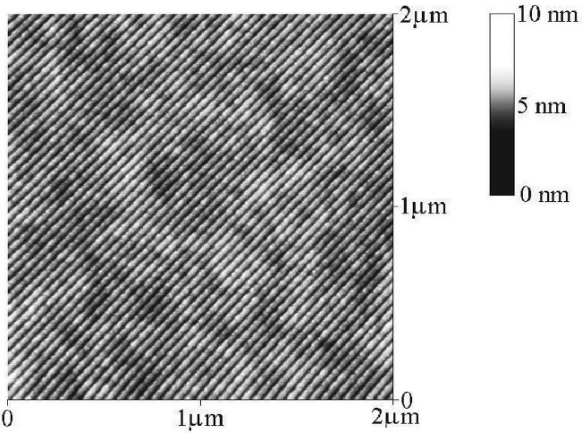

Fig. 24.9. Typical AFM image of a nanolithographed PMMA region. The scan size was 20 μm and the number of lines was 512

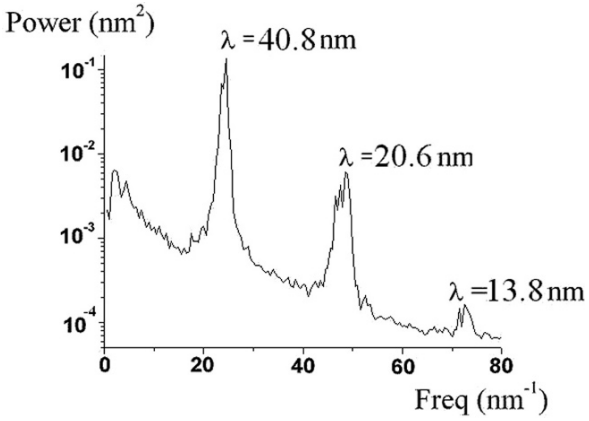

Fig. 24.10. Power spectral density of the image shown in Fig. 24.9

In some samples, the nanolithographed region shows a fine structure as can be seen in Fig. 24.13. In the AFM image of Fig. 24.13, aligned particles can be seen between the lines produced by the tip scratches. This image suggests that particles present in the developed PMMA [56, 57] are aligned during the nanolithography process.

Five samples were prepared nanolithographing the PMMA surface with 40-μm scan size and 512 lines and thus with distance between scan lines 78.1 nm. In all samples the morphological wavelengths obtained were: 78, 39, 26 and 20 nm (see Fig. 24.14). Note that 39 nm is half the distance between scan lines and 20 is about a quarter of the distance between scan lines. The 26-nm wavelength is probably related to fine structure of the developed PMMA.

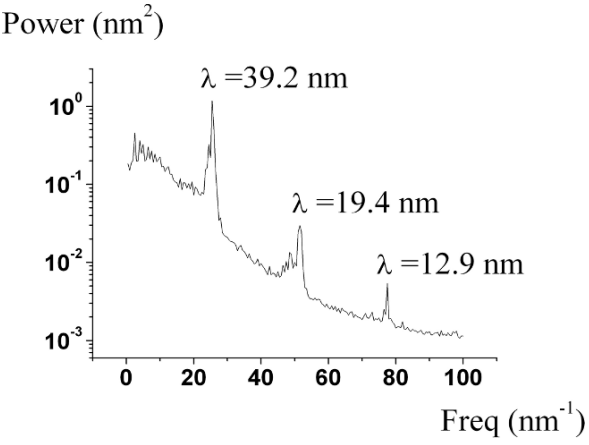

Fig. 24.11. PSD sum of nine different samples nanolithographed with 20-μm scan size and 512 lines

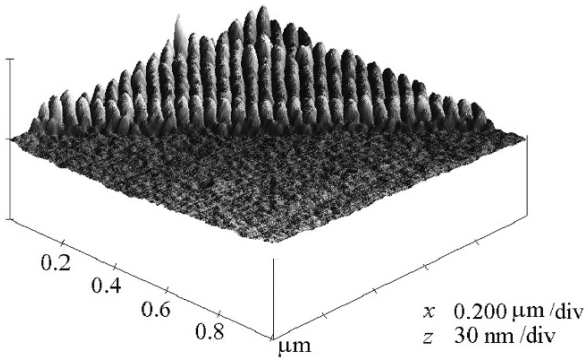

Fig. 24.12. AFM image of a border of the PMMA region nanolithographed using 20-μm scan size and 512 lines

In addition, five samples were nanolithographed with 30-μm scan size and 512 lines, generating distance between scan lines of 58.6 nm. In all samples a morphological wavelength of about 53 nm was present. In three of the samples a wavelength around 26 nm was observed, about half of the distance between scan lines.

Several more samples were prepared with different parameters, such as 10-μm scan size and 512 lines, and 20-μm scan size and 256 lines. Table 24.2 summarizes all the experimental results, showing the parameters used and the morphological wavelengths obtained.

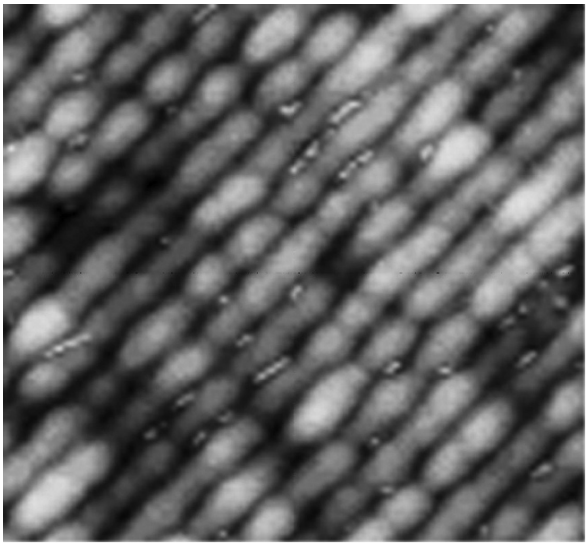

Fig. 24.13. AFM image of a nanolithographed PMMA with 20-μm scan size and 512 lines. A fine structure is present, where aligned particles can be observed. The image width is 500 nm

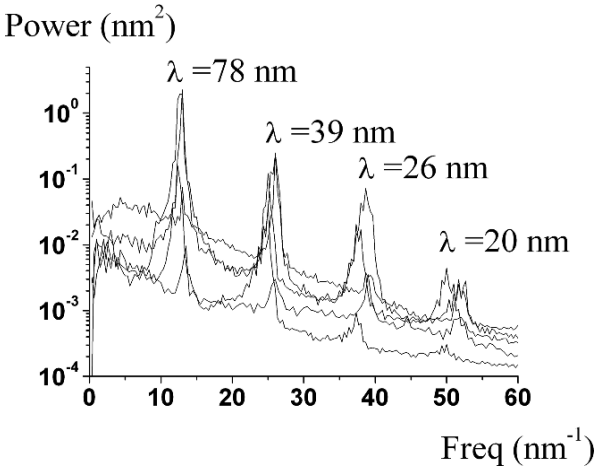

Fig. 24.14. PSD of five different samples nanolithographed with 40-μm scan size and 512 lines

A possible reason for morphological wavelengths of a quarter of the distance between scan lines is illustrated in Fig. 24.15. In the process of moving material from the region where the tip scratches the surface to the side of this region, depressions are created between the lines. In this way, the process introduces a new periodicity with wavelength of about one-fourth of the distance between lines (actually one-half of the distance between scratched lines).

Summarizing, nanolithography performed using an AFM generated reproducible and predictable periodicities, which were mainly dependent on the scan size and the number of scan lines. Power Spectral Density characterization was a powerful method for identifying the morphological wavelengths present in the nanolithography patterns.

Table 24.2. Summary of results. Scan size, number of lines, distance between lines, and morphological wavelengths present in the patterns formed

Scan size (μm)	Number of lines	Distance between lines (nm)	Morphological wavelength (nm)
10	512	19.5	18.7
20	512	39.1	39.2, 19.4
20	256	78.1	76.9, 39.2, 26.0, 19.6
30	512	58.6	53, 26
40	512	78.1	78.7, 39.2, 25.9, 19.6

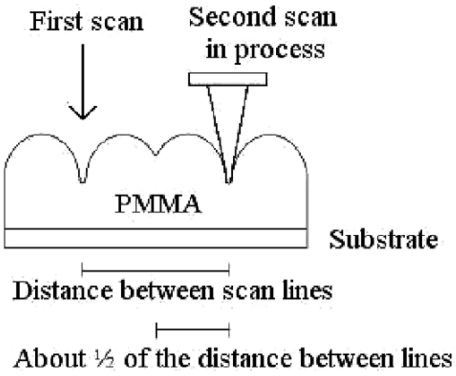

Fig. 24.15. Schematic suggesting the origin of wavelengths of one-quarter the distance between scan lines. The figure is not in scale

24.3.3 Electrical Resistivity of Nanostructured Thin Films

The electrical resistivity (ρ) of thin films involves quantum effects when two conditions are satisfied. The first is that the film thickness (d) must be smaller than the electronic mean-free-path (ℓ_0), and the second condition is that the energy-level quantization must be enhanced in the direction along the film thickness d. This last condition occurs when we have a small number of Fermi subbands, given by $N \cong d\left(\frac{3n}{\pi}\right)^{\frac{1}{3}}$, where n is the number of free electrons per unit volume.

For the specific case of platinum and gold films, these two conditions can be satisfied for very thin films [58], as shown in Table 24.3. The film thicknesses $d \leq \ell_0$ and the number of Fermi subbands, for the thickness used, was small (between 5 and 47). Thus, quantum effects are expected in determining the electrical resistivity of these thin films.

In the quantum model the calculation of the conductivity ($\sigma = 1/\rho$) as a function of the film thickness is done considering energy $E_v = \frac{\pi^2\hbar^2 v^2}{2md^2}$ quantization of the conduction electrons in the direction along the film thickness d in the Boltzmann transport equation, taking into account the distribution function of the Fermi sub-

Table 24.3. Conditions for applicability of a quantum formalism for platinum and gold thin films

Metal	Conditions for quantum formalism			
	Condition (I)		Condition (II)	
	d (nm)	ℓ_0 (nm)	n (m^{-3})	N
Pt	$1.3 \leq d \leq 11.7$	~ 10	6.6×10^{28}	$5 < N < 47$
Au	$1.8 \leq d \leq 10.5$	~ 50	5.9×10^{28}	$7 < N < 41$

bands ν and the scattering potential $U(x, y)$ due to the film morphology. Then the conductivity generated by the surface is given by [58]:

$$\sigma_s(d) \approx \frac{e^2}{\hbar} \frac{d^5}{2\pi^6 \Delta^2 F_S} \frac{6}{N(N+1)(2N+1)} \sum_{\nu=1}^{N} \frac{k_\nu^2}{\nu^2}$$

where Δ is the roughness of the film surface, $k_\nu^2 = \frac{2m}{\hbar^2}(E_F - E_\nu)$ are the wave numbers associated with the quantization in the direction along the film thickness d, and F_S is a function that depends on the interaction between the conduction electrons and the film surface morphology.

As will be detailed below, F_S depends on a characteristic interaction distance (ℓ_s) and on the film morphology. Thus, in this case, the film surface morphology must be quantified. For this purpose the film surface is represented by height fluctuations given by $z(x, y) = \pm\frac{d}{2} + h(x, y)$.

The film surface height fluctuations $h(x, y)$ generate a scattering potential given by $U \approx \left(\frac{\partial E}{\partial d}\right) h(x, y) = \frac{\pi^2 \hbar^2 \nu^2}{m\, d^3} h(x, y)$ and the conduction electron scattering is calculated from the transition probability given by: $|<k\nu|U(x, y)|k'\mu>|^2$.

The conduction electron scattering by the surface is calculated [58] taking into account an average interaction distance (ℓ_s):

$$\ell_s(\mathrm{d}) \approx v_{//}\tau_\mathrm{c},$$

where $\mathrm{v}_{//}$ is the velocity parallel to the surface (x,y) and τ_c is the collision time, corresponding to the time that the electron interacts with the surface during the collision. It is possible to calculate $\mathrm{v}_{//}$ using the conduction electron velocity in the z direction v_z and the Fermi velocity v_F:

$$v_{//}^2 = v_F^2 - v_z^2, \text{ where } v_F = \frac{\hbar}{m}\left(3\pi^2 n\right)^{1/3} \text{ and } v_z = \frac{\pi\hbar\nu}{md}.$$

The collision time is given by $\tau_c \approx {}^{d}/_{\mathrm{v}_z}$. Then the average interaction distance can be written as:

$$\ell_s(\mathrm{d}) = \; < \frac{v_{//}}{v_\mathrm{z}} > \mathrm{d} = \left(\frac{\pi}{3\mathrm{n}}\right)^{1/3} \sum_{\nu} \left[\left(\frac{3\mathrm{n}}{\pi}\right)^{2/3} \left(\frac{\mathrm{d}}{\nu}\right)^2 - 1\right]^{1/2}. \tag{24.2}$$

This quantity has been calculated for platinum and gold [58] thin films, showing an almost linear relationship between ℓ_s and d.

The morphology contribution to F_S is through the grain factor $g(d)$ that will be defined below.

At this point it is necessary to represent the film surface $h(x, y)$ as a Fourier expansion given by $h(x, y) = \Sigma_n\, h_n\, \sin(2\pi r/\lambda_n)$ [14,58–65], where r is the position vector modulus in the (x,y) plane given by $r = \sqrt{(x^2 + y^2)}$, λ_n is the morphological wavelength present in the surface, and h_n is the amplitude associated with each λ_n.

Specifically for the platinum and gold calculations, the morphological wavelengths λ_n were taken to be [14, 65] the film grain sizes D_n, so $\lambda_n \approx D_n$, and the wavelengths λ_n are given by an integer number of Fermi wavelengths $\lambda_n = \mathrm{n}\,\lambda_F$.

With this approach, F_S is given by $F_S(g, \ell_s) = g(d)\ \ell_s(d)$, where $\ell_s(d)$ is given by Eq. (24.2) and the grain factor is given by [58–64]:

$$g(d) = \frac{1}{k_F} \sum\nolimits_n (h_n/\Delta)^2\ (\lambda_F/\lambda_n)^2 \tag{24.3}$$

where k_F is the Fermi wavenumber and h_n and λ_n are associated with the Fourier expansion of the film surface height fluctuations.

For the case of metals, where $N >> 1$, the total film resistivity is given by $\rho(d) = \rho_{bulk} + \rho_s(d)$, and is given in terms of the quantities defined above by [59]:

$$\frac{\rho(d)}{\rho_{bulk}} = 1 + \frac{C\Delta(d)^2\ g(d)\ \ell_s(d)}{d^2(1 - 0.15/d)}$$

where C is a constant that depends of the material, and specifically for platinum and gold is equal to $C_{\mathrm{Pt}} = 6.261 \times 10^3\,\mathrm{nm}^{-2}$ and $C_{\mathrm{Au}} = 28.072 \times 10^3\,\mathrm{nm}^{-2}$, $\Delta(d)$ is the roughness measured as a function of the thickness d, $g(d)$ is obtained from Eq. (24.3) measuring the morphological grain sizes as a function of the thickness d, and $\ell_s(d)$ is calculated as given in Eq. (24.2).

The distinction between morphological and crystallographic grain sizes will be discussed later in this text.

With this model, the platinum and gold resistivities were calculated for film thickness between 1 and 10 nm [60]. The calculated values were found to be in excellent agreement with the experimental data, as shown in Fig. 24.16.

On the basis of these results, it was further proposed that morphological anisotropy of the film surface should induce an associated anisotropy in the resistivity [61]. To estimate the metric scale needed for this effect to be manifested experimentally, the theory described above was used to calculate the resistivity of a simple surface with anisotropic morphology.

The geometry used for this estimate was similar to that shown in Fig. 24.1 of this chapter. The surface was defined by a sinusoidal profile in the x-direction given by $z = h \sin(2\pi x/L)$, where h is the amplitude of the sinusoidal profile and L the morphological wavelength. A granular profile was assumed in the y-direction instead

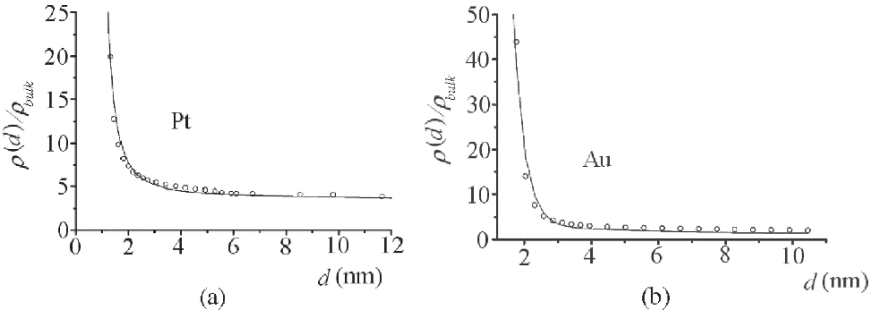

Fig. 24.16. Measured (*circles*) and calculated (*continuous line*) [60] resistivities for (**a**) platinum and (**b**) gold thin films. The fit is excellent

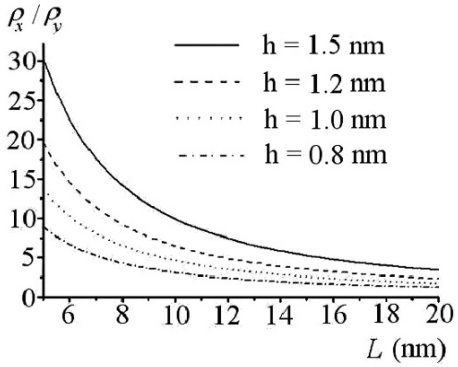

Fig. 24.17. Anisotropy factor ρ_x/ρ_y as a function of morphological surface wavelength L. Each curve corresponds to different amplitude of the sinusoidal surface profile

of a flat profile, as nanostructured thin films usually are when formed by filtered vacuum arc plasma deposition.

The results of the calculation are shown in Fig. 24.17, where the anisotropic factor ρ_x/ρ_y is given as a function of different morphological surface wavelengths L and each curve corresponds to different amplitudes of the sinusoidal surface profile between $h = 0.8\,\mathrm{nm}$ and $h = 1.5\,\mathrm{nm}$.

In this calculation gold was taken as the film material and the average thickness was 5 nm.

As is clear from Fig. 24.17, the morphological wavelength L that is required in order for the anisotropic resistivity effect to be experimentally observable is too small (several nanometers) to be nanofabricated on the surface.

We have investigated an alternative approach for creating an anisotropic surface morphology. The substrate was a glass microscope slide scratched in one direction with $1/4$-$\mu\mathrm{m}$ diamond powder dispersed in water [61]. Figure 24.18 shows an AFM image of the glass surface with anisotropic morphology.

Two substrates were cut from a single scratched sample as indicated in Fig. 24.19. In this way substrate A has grooves in the longitudinal (y) direction and substrate B has grooves in the transverse (x) direction. Electrical contacts were formed on both ends of the substrates using silver glue followed by plasma deposition of relatively thick ($\sim$200 nm) platinum films onto the contacts, with a mask protecting the center of the sample, as shown in Fig. 24.19. Both substrates were then positioned in the plasma deposition vacuum chamber and their resistance measured throughout the platinum film deposition process. The film resistance was measured after the first six pulses of the repetitively pulsed plasma deposition process and subsequently after every three pulses, thus determining film resistance as a function of film thickness without removing the sample from vacuum for each individual measurement.

The films were formed by filtered vacuum arc plasma deposition [66–69] and the chosen material was platinum. The resistivity, ρ, was determined from the measured resistance R_m from $\rho = (R_m - R_c)dw/\ell$, where w and ℓ are the sample width and length, respectively, and R_c is an estimated contact resistance. The

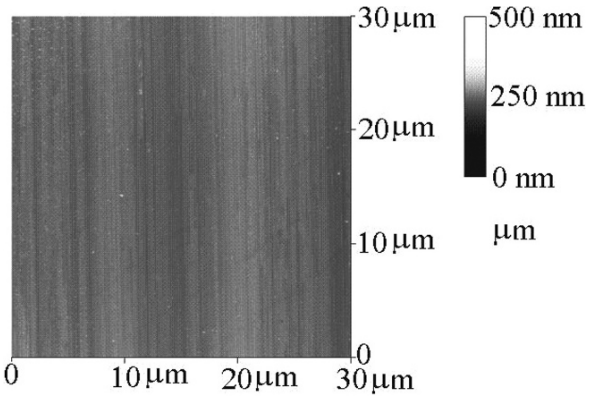

Fig. 24.18. AFM image of glass substrate surface after scratching with 1/4-μm diamond powder, showing the morphological anisotropy

measured resistance values varied over the range 2.5 MΩ to 15 Ω and the contact resistance was about 5Ω. Noting that the contact resistance is constant during the experimental measurements and that the highest resistances (∼MΩ) were measured for the thinnest films, it is clear that the contact resistance is irrelevant for these very thin films. The platinum film resistivity spanned the range 12 to 1.2 Ω. m. The measured longitudinal and transverse resistivities, ρ_y and ρ_x respectively, are shown in Fig. 24.20 as a function of film thickness d. The resistivity of both samples increases with decreasing film thickness, as expected for very thin films [58–64].

The resistivity anisotropy ratio $\rho_x(d)/\rho_y(d)$ is shown in Fig. 24.21 as a function of film thickness, and is greater than unity and varies with thickness. The resistivity anisotropy increases significantly for film thickness less than about 2 nm, up to greater than a factor of 10 for the thinnest films investigated of thickness 0.4 nm. We point out parenthetically that the anisotropy ratio ρ_x/ρ_y is expected to reach near unity only for thicknesses d greater than about 70 nm [70, 71], which is consistent with an extrapolation of the Fig. 24.21 data that indicates about 90 nm.

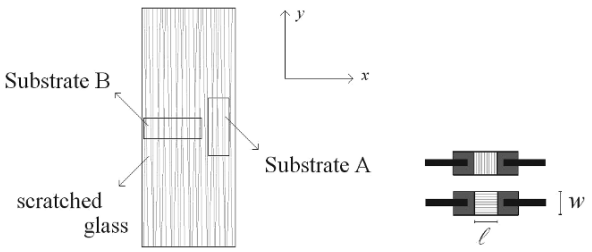

Fig. 24.19. Schematic showing preparation of samples A and B from the scratched glass substrate; substrate A is grooved in the longitudinal or y-direction, and substrate B is grooved in the transverse or x-direction. A schematic of the finished samples is shown on the right

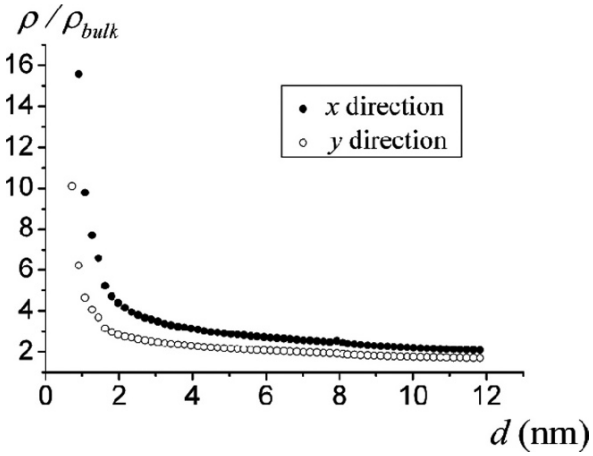

Fig. 24.20. Measured resistivity ratios ρ_x/ρ_{bulk} and ρ_y/ρ_{bulk} as a function of film thickness

These results indicate a significant resistivity anisotropy that is a consequence of the film morphological anisotropy, attesting to the importance of quantitative morphological analysis for this area.

Summarizing, according to our studies on platinum and gold thin film resistivities, we have shown [58–64] that the conduction electrons are scattered by the surface morphology. We have demonstrated that the quantitative morphological analysis of the films surface is a very important parameter and must be taken into account.

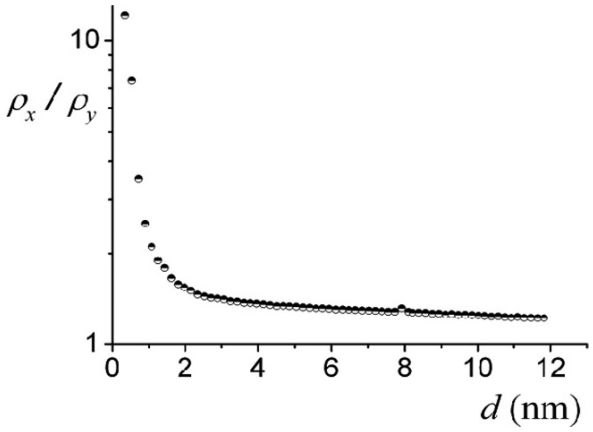

Fig. 24.21. Measured resistivity anisotropy ratio ρ_x/ρ_y as a function of film thickness d

24.3.4 Morphological and Crystallographic Grain Sizes

A number of applications of morphological surface analysis have been discussed in the above, including the importance of grain size determination for thin film resistivity.

A very common way to measure grain size is by using X-ray diffraction [72]. This technique allows measurement of an average grain size over the analyzed region, which can be two or three orders of magnitude larger than the area analyzed in one SPM image. In the following we discuss the distinction between morphological and crystallographic grain size and the importance of morphological grain analysis.

The crystallographic and morphological grain sizes for the platinum and gold thin films have been measured as a function of film thickness d using two different techniques: X-ray diffraction and STM [73].

Typical top-view STM micrographs of platinum and gold films are shown in Figs. 24.22 and 24.23. Figure 24.22 shows platinum films (a) 5 nm thick, and (b) 155 nm thick. Figure 24.23 shows gold films (a) 38 nm thick, and (b) 200 nm thick. These images clearly show the nanostructured nature of the films and how the granular structure changes with film thickness. It can also be seen that the surfaces are composed of different grain sizes. These surfaces have a characteristic fractal auto-affine symmetry [1, 4] with a "cauliflower morphology," where larger grains are composed of aggregates of smaller grains. The "grain diameter" or "grain size" D measured topographically on the film surface is the "morphological grain size." The grain dimension D_c measured by X-ray diffraction [72] is called the "crystallographic grain size." Thus, the morphological grain size is the grain dimension exposed in the film surface; and crystallographic grain size is the grain dimension imbedded in the film bulk.

The analyzed films were deposited by filtered vacuum arc plasma deposition [66–69]. Two kinds of substrates were used—monocrystalline silicon and an ordinary glass microscope slide. The second substrate, being amorphous, allows us to

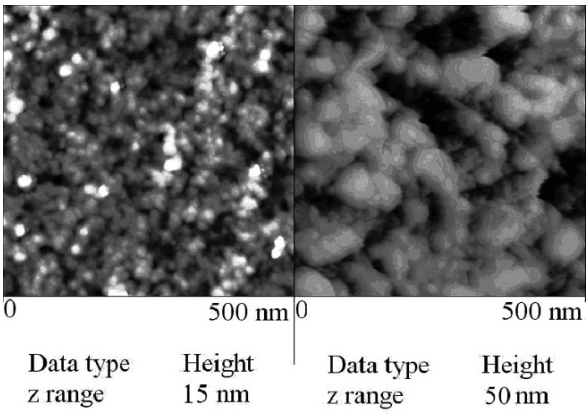

Fig. 24.22. STM images of Pt thin film: (**a**) 5 nm thick, and (**b**) 155 nm thick

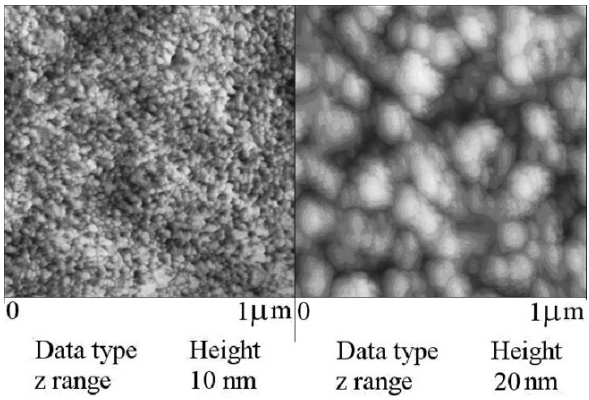

Fig. 24.23. STM images of Au thin film: (**a**) 38 nm thick, and (**b**) 200 nm thick

check whether or not any preferential film crystallographic orientation is induced by the substrate epitaxy.

The thickness d of the films was measured by placing a small piece of silicon close to the sample, with an ink mark that was removed after deposition and the step-height then measured by AFM.

The film thickness $d(t)$ was determined as a function of deposition time t for the platinum and gold films. The thickness increases linearly with time and the deposition rate was measured to be 7.6 nm/s for platinum and 29.6 nm/s for gold.

Characterization techniques used were STM for the morphological grain size and X-ray diffraction for crystallographic grain size and orientation.

The microscope used was a Scanning Probe Microscope, Veeco Nanoscope IIIA, in STM mode. Commercial platinum-iridium (STM) tips and homemade tungsten tips were used. About four different regions were imaged for each sample. The scan size was between 200 nm and 1 μm, with 512×512 pixels for the image resolution.

The X-ray diffraction measurements were carried out in a Rigaku diffractometer, with a $0.05°$-step. The Cu-λK_α beam was produced by a conventional X-ray generator and monochromatized with a graphite crystal. The crystallographic grain size D_c was evaluated by the Scherrer equation [72].

Figures 24.22 and 24.23 show typical top view STM images of platinum and gold thin films, respectively. This kind of micrograph was used to measure the morphological grain sizes. Initially, the grain boundaries were defined and after their sizes D were measured. For each film with thickness d, the number of grains $N(D)$ of dimension D were plotted in histograms as a function of D. The D range, $D_{\min} \leq D \leq D_{\max}$ depends on the film thickness. The minimum grain size $D_{\min}$ was limited basically by the resolution of the micrographs, since the pixel size used was between 0.4 and 2 nm. Because of this limitation, we took $D_{\min} \geq 3$–5 nm for platinum and gold films, independent of the thickness d. On the other hand, $D_{\max}$ increases as d increases. A typical $N(D)$ histogram is shown in Fig. 24.24 for a gold film with $d = 3$ nm. The continuous curve represents the histogram best fit. From these histograms were determined the average grain dimensions. Note that in the

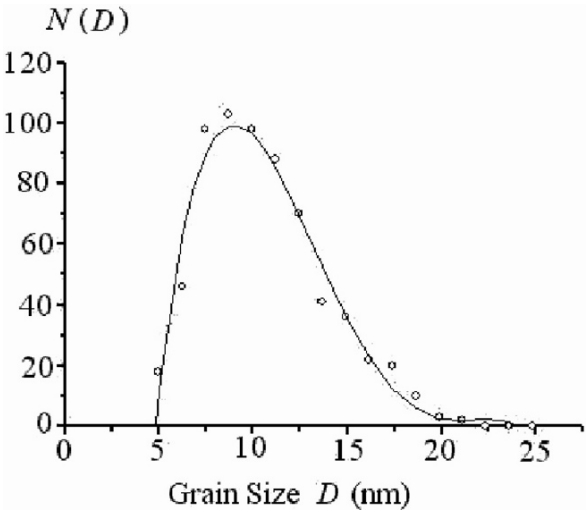

Fig. 24.24. Histogram of the morphological grain sizes $D(d)$ for a Au film 3-nm thick

histograms, there is always a sharp cutoff for smaller grains. This is due to the image resolution mentioned above.

The average values of the crystallographic and morphological grain sizes for each thickness d are indicated in the following by $D_c(d)$ and $D(d)$, respectively.

The morphological and crystallographic grain size analyses yield similar results for the silicon and glass substrates, within experimental error. Thus, in the following we do not distinguish between the substrate used for each sample analyzed.

In Fig. 24.25 the $D_c(d)$ values are plotted as a function of d. For platinum, the experimental results are indicated by open circles and for gold by solid circles. One can see from these figures that the grain size $D_c(d)$ saturates for large thickness [71]. For platinum films the saturation occurs at $d \approx 100\,\mathrm{nm}$, with a maximum grain size of around 23 nm. For gold films the saturation occurs at $\mathrm{d} \approx 140\,\mathrm{nm}$, with a maximum grain size of around 48 nm.

X-ray analysis confirmed that both platinum and gold films grow preferentially in the (111) direction. This effect was observed for both the silicon and glass substrates, showing that it is not an epitaxial effect. This implies that the films growth process is self-oriented.

The average morphological grain size $D(d)$, for platinum and gold, as a function of d is plotted in Fig. 24.26 in the form $\log[D(d)]$ vs. $\log(d)$. In both cases $D(d)$ increases rapidly in the region with thickness $d < 4\,\mathrm{nm}$. In the range $4 < d < 45\,\mathrm{nm}$, $D(d)$ is constant at $D(d) \approx 13 \sim 15\,\mathrm{nm}$. For thickness $2 < d < 45\,\mathrm{nm}$, $D(d)$ can be approximately described by the functions

$$D_{Pt}(d) \approx 15.5\{1 - 1.1\exp(-0.9d^{1.8}) - 2.3\exp[-0.001(d-45)^2]\} \text{ and}$$

$$D_{Au}(d) \approx 12.8\{1 - 3\exp(-0.7d^{1.8}) - 2.3\exp[-0.001(d-40)^2]\}.$$

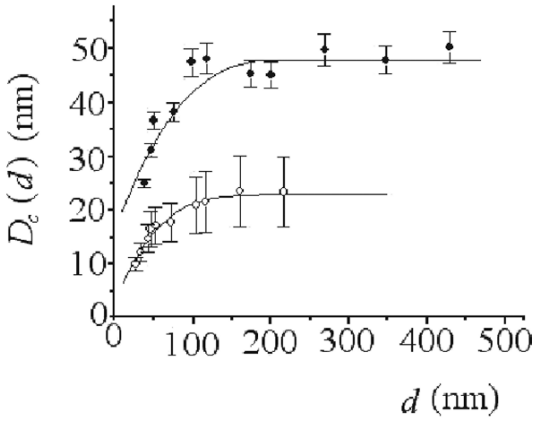

Fig. 24.25. Average crystallographic grain size $D_c(d)$ as a function of film thickness d, for Pt and Au films. The experimental results are indicated by open circles for Pt and by solid circles for Au

For $d > 45\,\mathrm{nm}$, $D(d)$ increases with d and can be represented for both platinum and gold by $D(d) \approx 10.50 + 0.0334\ d + 0.0022\ d^2$. These results show that for $d > 45\,\mathrm{nm}$ the morphological grain size $D(d)$ increases with d, as distinct from the crystallographic grain size $D_c(d)$ which saturates. This can be understood considering that for X-ray diffraction, crystalline defects are detected as grain boundaries, and thus the $D_c(d)$ saturation can be interpreted as high-density crystallographic defects. Figure 24.27 shows a three-dimensional micrograph view of a gold film 200-nm thick. This image suggests that the morphological grains are agglomerates of crystallographic grains, exemplifying the concept described above.

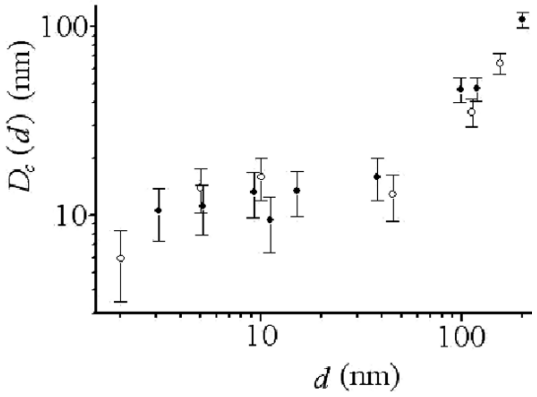

Fig. 24.26. Average morphological grain size $D(d)$ as a function of film thickness d, for Pt and Au films. The experimental results are indicated by open circles for Pt and by solid circles for Au

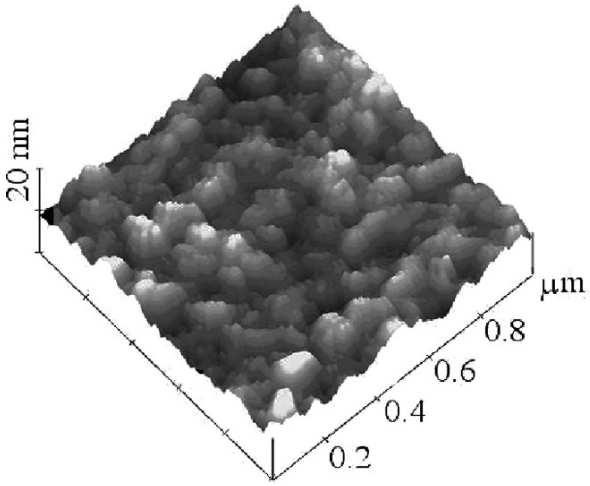

Fig. 24.27. Three-dimensional view of STM image of a gold film 200-nm thick

The early growth is generally subdivided into three main categories: (a) layer-by-layer growth, where a continuous monolayer is preferentially formed prior to the deposition of the subsequent layer; (b) island growth, where the deposition atoms tend to aggregate into island growth with thickness of several monolayers; and (c) mixed mode [66]. For the platinum and gold films described here, the early growth is in islands. Note that the thinner films analyzed here must be conductive enough to allow STM images to be obtained, this implies that the films have already coalesced.

Summarizing, nanostructured platinum and gold thin films with thickness between 2 and 430 nm have been fabricated by filtered vacuum arc plasma deposition. The films were analyzed measuring the morphological and crystallographic grain sizes as a function of film thickness. It was observed that for both platinum and gold films the crystallographic grain size saturates for large thickness and that they grow preferentially in the (111) direction. This effect was observed for both silicon and glass substrates, indicating that the film growth process is self-oriented. The morphological grain size, for platinum and gold films, increases monotonically except in the range of thickness between 4 and 45 nm, where the grain size saturates. The results show that for $d > 45\,\mathrm{nm}$ the morphological grain size $D(d)$ increases with d, distinct from the crystallographic grain size $D_c(d)$ which saturates. This can be understood by considering that for X-ray diffraction, crystalline defects are detected as grain boundaries, so the $D_c(d)$ saturation could be interpreted as high-density crystallographic defects. Concerning the early growth of the films, the films grow as islands, but the thinner films analyzed must be conductive enough to allow STM images to be obtained; this implies that the films have already coalesced.

The explanation above defined “morphological grain size” as the grain dimension exposed on the film surface, and “crystallographic grain size” as the grain dimension

imbedded in the film bulk. The importance of the morphological grain size has been pointed out by several workers.

As discussed in this text as the third application of quantitative analysis of surface morphology, the quantum theory applied to the electrical resistivity of nanostructured thin films [58–64] makes use of the morphological grain size as an important parameter.

Thermoelectric power in very thin films has been also studied [74,75], taking into account quantum size effects. In this study, the electrical resistivity theory [58–64] was successfully used, meaning that the morphological grain size was an important parameter in this case also.

24.4 Final Remarks

Quantitative analysis of surface morphology is an extensive field and it has not been our intension to discuss it in all possible facets. A number of significant parameters have been presented and four applications have been described where quantitative morphological analyses were required. Importantly, note that the SPM technique is fundamental for quantitative morphological analysis since it allows imaging surfaces with precise measurement in three dimensions.

Acknowledgments. The author would like to thank Professor Ian G. Brow, from Lawrence Berkeley National Laboratory, and Professor Mauro S. D. Cattani, from University of Sao Paulo, for the critical reading of this Chapter. This work was supported by Fundação de Amparo a Pesquisa do Estado de São Paulo (FAPESP), the Conselho Nacional de Desenvolvimento Científico e Tecnológico (CNPq) and the Coordenação de Aperfeiçoamento de Pessoal de Nível Superior (Capes), Brazil.

References

1. Barabási AL, Stanley HE (1995) Fractal concepts in surface growth. Cambridge University Press, Cambridge
2. Salvadori MC, Martins DR, Cattani M (2006) Surf Coat Technol 200:5119
3. Cattani M, Salvadori MC (2005) Surf Rev Lett 12:675
4. Melo LL, Salvadori MC, Cattani M (2003) Surf Rev Lett 10:903
5. Salvadori MC, Melo LL, Cattani M, Monteiro OR, Brown IG (2003) Surf Rev Lett 10:1
6. Salvadori MC, Melo LL, Martins DR, Vaz AR, Cattani M (2002) Surf Rev Lett 9:1409
7. Cattani M, Salvadori MC (2001) Surf Rev Lett 8:347
8. Salvadori MC, Pizzo Passaro AM, Cattani M (2001) Surf Rev Lett 8:291
9. Cattani M, Salvadori MC (2000) Thin Solid Films 376:264
10. Pizzo Passaro AM, Salvadori MC, Martins DR, Cattani M (2000) Thin Solid Films 377–378:285
11. Salvadori MC, Silveira MG, Cattani M (1999) Thin Solid Films 354:1
12. Salvadori MC, Silveira MG, Passaro AMP, Cattani M (1998) Acta Microscopica 7:465
13. Palasantzas G, Zhao YP, Wang GC, Lu TM (2000) Phys Rev B 61:11109
14. Feder J (1988) Fractals. Plenum Press

15. Family F, Vicsek T (1985) J Phys A 18:L75
16. Kardar M (1996) Physica B 221:60
17. Kim J, Palasantzas G (1995) Int J Mod Phys B 9:599
18. Salvadori MC, Silveira MG, Cattani M (1998) Phys Rev E 58:6814
19. Salvadori MC, Mammana VP, Martins OG, Degasperi FT (1995) Plasma Sources Sci Technol 4:489
20. Salvadori MC, Ager JW III, Brown IG, Krishman KM (1991) Appl Phys Lett 59:2386
21. Bevington PR (1969) Data reduction and error analysis for the physical sciences. McGraw-Hill, New York
22. Kardar M, Parisi G, Zhang YC (1986) Phys Rev Lett 56:889
23. Kardar M, Zhang YC (1987) Phys Rev Lett 58:2087
24. Medina E, Hwa T, Kardar M (1989) Phys Rev A 39:3053
25. Hwa T, Kardar M, Paczuski M (1991) Phys Rev Lett 66:441
26. Baur C, Bugacov A, Koel BE, Madhukar A, Montoya N, Ramachandran TR, Requicha AAG, Resch R, Will P (1998) Nanotechnology 9:360
27. Beton PH, Dunn AW, Moriarty P (1995) Appl Phys Lett 67:1075
28. Cuberes MT, Schlitter RR, Gimzewski JK (1996) Appl Phys Lett 69:3016
29. Teixeira FS, Mansano RD, Salvadori MC, Cattani M, Brown IG (2007) Rev Sci Instrum 78:053702
30. Chen J-M, Liao S-W, Tsai Y-C (2005) Synthetic Metals 155:11
31. Magno R, Bennett BR (1997) Appl Phys Lett 70:1855
32. Bouchiat V, Esteve D (1996) Appl Phys Lett 69:3098
33. Sohn LL, Willett RL (1995) Appl Phys Lett 67:1552
34. Hu S, Altmeyer S, Hamidi A, Spangenberg B, Kurz H (1998) J Vac Sci Technol B 16:1983
35. Kunze U, Klehn B (1999) Adv Mater 11:1473
36. Klehn B, Kunze U (1999) J Appl Phys 85:3897
37. Mamin HJ, Rugar D (1992) Appl Phys Lett 61:1003
38. Mamin HJ (1996) Appl Phys Lett 69:433
39. Snow ES, Campbell PM (1994) Appl Phys Lett 64:1932
40. Tsau L, Wang D, Wang KL (1994) Appl Phys Lett 64:2133
41. Campbell PM, Snow ES, McMarr PJ (1995) Appl Phys Lett 66:1388
42. Fontaine PA, Dubois E, Sti'evenard D (1998) J Appl Phys 84:1776
43. Dai H, Franklin N, Han J (1998) Appl Phys Lett 73:1508
44. Wilder K, Quate CF (1998) Appl Phys Lett 73:2527
45. Park SW, Soh HT, Quate CF, Park S-I (1995) Appl Phys Lett 67:2415
46. Tully DC, Wilder K, Fr'echet JMJ, Trimble AR, Quate CF (1999) Adv Mater 11:314
47. Piner RD, Zhu J, Xu F, Hong S, Mirkin CA (1999) Science 283:661
48. Hong S, Zhu J, Mirkin CA (1999) Science 286:523
49. Lee KB, Park S-J, Mirkin CA, Smith JC, Mrksich M (2002) Science 295:1702
50. Li Y, Maynor BW, Liu J (2001) J Am Chem Soc 123:2105
51. Maynor BW, Filocamo SF, Grinstaff MW, Liu J (2002) J Am Chem Soc 124:522
52. Jang SY, Marquez M, Sotzing GA (2004) J Am Chem Soc 126:9476
53. Sader JE (1995) Rev Sci Instrum 66:4583
54. Pratt WK (2001) Digital image processing: PIKS, 3rd edn John Wiley & Sons; New York
55. Command Reference Manual, Software version 5.12r3, Nanoscope IIIa, Veeco
56. Dobisz EA, Brandow SL, Snow E, Bass R (1997) J Vac Sci Technol B 15:2318
57. Dobisz EA, Brandow SL, Bass R, Shirey LM (1998) J Vac Sci Technol B 16:3695
58. Cattani M, Salvadori MC (2004) Surf Rev Lett 11:283
59. Cattani M, Vaz AR, Wiederkehr RS, Teixeira FS, Salvadori MC, Brown IG (2007) Surf Rev Lett 14:87
60. Salvadori MC, Vaz AR, Farias RJC, Cattani M (2004) Surf Rev Lett 11:223

61. Salvadori MC, Cattani M, Teixeira FS, Wiederkehr RS, Brown IG (2007) J Vac Sci Technol A 25:330
62. Cattani M, Salvadori MC (2004) Surf Rev Lett 11:463
63. Cattani M, Salvadori MC, Teixeira FS, Wiederkehr RS, Brown IG (2007) Surf Rev Lett 14:345
64. Cattani M, Salvadori MC, Filardo Bassalo JM (2005) Surf Rev Lett 12:221
65. Namba Y (1970) Jpn J Appl Phys 9:1326
66. Anders A (ed) (2000) Handbook of plasma immersion ion implantation and deposition. John Wiley & Sons, Inc, New York
67. nders A (1997) Surf Coat Technol 93:158
68. Monteiro OR (1999) Nucl Instrum Methods Phys Res B148:12
69. Brown IG, Anders A, Dickinson MR, MacGill RA, Monteiro OR (1999) Surf Coat Technol 112:271
70. Jalochowski M, Bauer E, Knoppe H, Lilienkamp G (1992) Phys Rev B 45:13607
71. Barnat EV, Nagakura D, Wang PI, Lu TM (2002) J Appl Phys 91:1667
72. Cullity BD (1978) Elements of X ray diffraction, 2nd edn. Addison-Wesley Publishing Company, Massachusetts
73. Salvadori MC, Melo LL, Vaz AR, Wiederkehr RS, Teixeira FS, Cattani M (2006) Surf Coat Technol 200:2965
74. Salvadori MC, Vaz AR, Teixeira FS, Cattani M, Brown IG (2006) Appl Phys Lett 88:133106
75. Cattani M, Salvadori MC, Vaz AR, Teixeira FS, Brown IG (2006) J Appl Phys 100:114905